The Astrophysical Journal, 865:141 (12pp), 2018 October 1 https://doi.org/10.3847/1538-4357/aadee8

EPIC 203868608: A Low-mass Quadruple Star System in the Upper Scorpius OB Association

Ji Wang[1,2], Trevor J. David[1,3], Lynne A. Hillenbrand[1], Dimitri Mawet[1], Simon Albrecht[4], and Zibo Liu[5]
[1] Department of Astronomy, California Institute of Technology, MC 249-17, 1200 E. California Boulevard, Pasadena, CA 91106, USA; ji.wang@caltech.edu
[2] Department of Astronomy, The Ohio State University, 100 W 18th Avenue, Columbus, OH 43210, USA
[3] Jet Propulsion Laboratory, California Institute of Technology, 4800 Oak Grove Drive, Pasadena, CA 91109, USA
[4] Stellar Astrophysics Centre, Department of Physics and Astronomy Aarhus University, Ny Munkegade 120, DK-8000, Aarhus C, Denmark
[5] Department of Astronomy & Key Laboratory of Modern Astronomy and Astrophysics in Ministry of Education, Nanjing University, 210093, People's Republic of China
Received 2018 July 2; revised 2018 August 31; accepted 2018 September 2; published 2018 October 3

Abstract

Young multiple star systems provide excellent testing grounds for theories of star formation and evolution. EPIC 203868608 was previously studied as a triple star system in the Upper Scorpius OB association, but the followup Keck NIRC2/HIRES/NIRSPAO observations reported here reveal its quadruple nature. We find that the system consists of a double-lined spectroscopic binary (SB2) Aab (M5+M5) and an eclipsing binary (EB) Bab with a total mass that is lower than that of the SB2. Furthermore, we measure the obliquity of the EB using the Doppler tomography technique during the primary eclipse. EPIC 203868608 Bab is likely on an inclined orbit with a projected obliquity of -57^{+40}_{-36} degrees. The inclined orbit is used to constrain the tidal quality factor for low-mass stars and the evolution of the quadruple system. The analytic framework to infer obliquity that has been developed in this paper can be applied to other EB systems as well as transiting planets.

Key words: binaries: close – binaries: eclipsing – binaries: spectroscopic – stars: late-type – stars: low-mass – techniques: radial velocities

1. Introduction

The stellar population in the solar neighborhood is dominated by multiple star systems, mostly binaries and some triples, but with 3% of stellar systems being quadruple and higher-order multiples (Raghavan et al. 2010). Despite being rare, the high-order multiple systems offer unique insight into the process of star formation (Mathieu 1994; Tohline 2002; Reipurth & Mikkola 2012; Duchêne & Kraus 2013), e.g., large-scale core or filament fragmentation (Pineda et al. 2015) versus small-scale disk fragmentation (Tobin et al. 2016).

Among multiple stellar systems, eclipsing systems are particularly interesting because they provide an opportunity to directly measure masses and radii. The *Kepler* mission (Borucki et al. 2010) greatly expanded the catalog of eclipsing binaries (EBs, Kirk et al. 2016). In addition, higher-order multiple eclipsing stellar systems have also been discovered by the *Kepler* mission (Carter et al. 2011; Derekas et al. 2011; Lehmann et al. 2012, 2016). After the *Kepler* mission, the repurposed *K2* mission (Howell et al. 2014) discovered even more high-order multiple eclipsing stellar systems (e.g., Alonso et al. 2015; Rappaport et al. 2016, 2017). In total, the *Kepler* satellite greatly expands upon previously known eclipsing multiple stellar systems by revealing more than 200 high-order EBs owing to its unprecedented photometric precision and long time baseline (Conroy et al. 2014; Borkovits et al. 2016). In the future, the *Transiting Exoplanet Survey Satellite* (*TESS*) mission (Ricker et al. 2014) and the PLATO mission (Rauer et al. 2014) will continue the trend of EB and transiting planet discoveries.

Notably, *K2* observations of the Upper Scorpius OB association have yielded a number of young eclipsing systems (Alonso et al. 2015; Kraus et al. 2015; Lodieu et al. 2015), including EPIC 203868608 (David et al. 2016, hereafter D16). The system previously was thought to be a hierarchical triple with a pair of eclipsing brown dwarfs. In this paper, however, we provide evidence that EPIC 203868608 is in fact a young quadruple system, consisting of a double-lined spectroscopic binary (SB2) and an EB. We show that all four stars are likely to have low masses ($\lesssim 0.3\,M_{\odot}$) and that the EB is likely to be on an inclined orbit.

We present our observations with a suite of instruments on the Keck telescopes in Section 2. Results are given in Section 3, including the stellar and orbital properties of EPIC 203868608. In Section 4, we focus on the obliquity of the EB in EPIC 203868608. The summary is given in Section 5.

2. Observation and Data Reduction

2.1. Keck/NIRC2

We observed EPIC 203868608 using the Keck/NIRC2 instrument (Wizinowich et al. 2000) in laser guide star (LGS) mode. LGS mode was required for an acceptable adaptive optics (AO) performance because EPIC 203868608 is faint in wavefront sensing wavelengths ($r = 16.3$ mag) and cannot serve as a natural guide star. We obtained AO images in the J and K_P bands at three epochs. The first two epochs of observations were obtained from the Keck Observatory Archive (PID: N121N2L, PI: Mann, and PID: H210N2L, PI: Baranec). The first epoch was taken during the primary eclipse (UT 2015 June 22, MJD 57195.42345). Since we set the orbital phase [0–1] to zero at the middle of the primary eclipse, the observation corresponded to an orbital phase of 0.9942. The second epoch was taken at UT 2015 July 25, MJD 57228.26646, corresponding to a orbital phase of 0.3674, when the total flux of the system is at a normal (non-eclipsing) level. We took the third epoch of observation on UT 2016 July 17 (PID: C237N2L, PI: Mawet) at an orbital phase of 0.4371, 2.94 hr from the secondary eclipse.

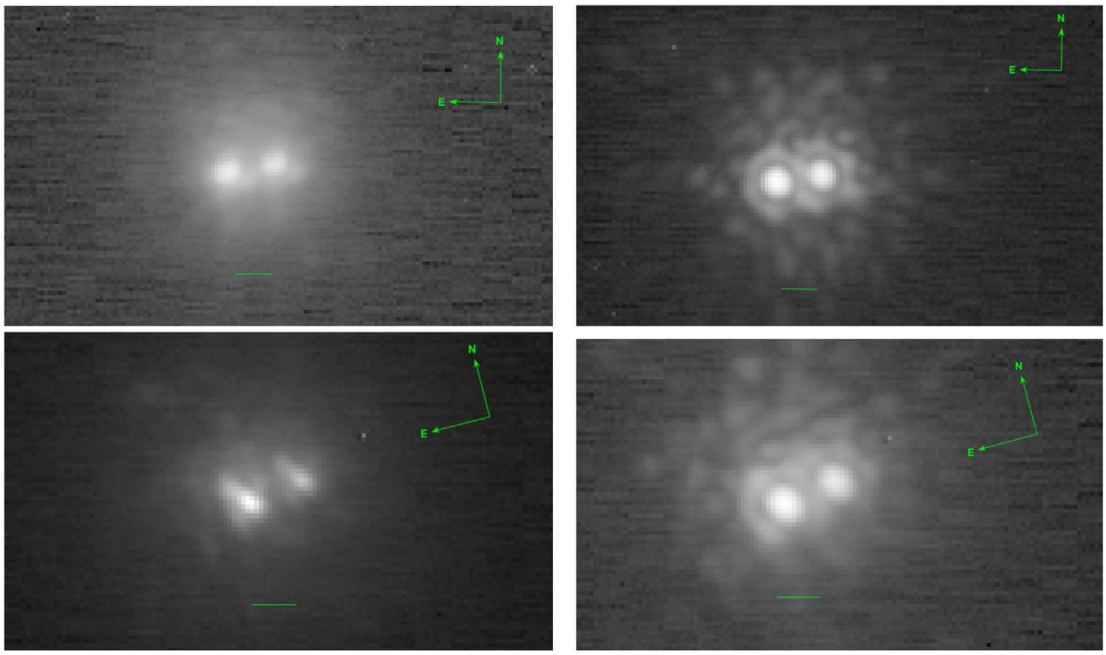

Figure 1. AO images for EPIC 203868608 in the J (left column) and K_P (right column) bands. Images are shown in logarithmic scale. A compass is shown to indicate north and east. The horizontal green bar in each plot shows 0.″1 scale. The top row show images of when B (the west component) is not eclipsed and the bottom row shows images of when B is during the primary eclipse.

Table 1
Summary of Observations

Instrument	UT Date	Wavelength	Exposure	Configuration	Seeing
NIRC2	2015 Jun 22[a]	J	40 s	Narrow	0.″6
		K_P	40 s	Narrow	
	2015 Jul 25[b]	J	90 s	Narrow	0.″3
		K_P	300 s	Narrow	
	2016 Jul 17	K_P	60 s	Narrow	0.″4
HIRES[c]	2015 Jun	3600	Varied	B2, C2, and	Varied
	2017 Jul	−9200 Å		C5 deckers	
NIRSPAO	2017 Jul 06	K	2.67 hr	AO	0.″9

Notes.
[a] Data from Keck Observatory Archive (KOA), PI: Mann.
[b] Data from KOA, PI: Baranec.
[c] See David et al. (2016) for more details.

On UT 2015 June 22, two J-band AO frames without dithering and two K_P-band AO frames with a dither pitch of 0.″27 were taken. The total on-target time per frame was 20 s (1 s with 20 coadds).

On UT 2015 July 25, three J-band AO frames were taken with a three-point dither pattern that has a throw of 2.″5. The lower left quadrant was avoided because it has a much higher instrumental noise than the other three quadrants on the detector. Total on-target time per frame in the J band was 30 s (1.25 s with 24 coadds). Five K_P-band AO frames were taken with a five-point dither pattern. The five-point dither pattern has the target in the center of the detector and the centers of each detector quadrant. The total on-target time per frame in K_P band was 60 s (1.25 s with 48 coadds).

On UT 2016 July 17, we took three K_P-band AO frames with a three-point dither pattern that has a throw of 2.″5. Total on-target time per frame was 20 s (2 s with 10 coadds). All Keck NIRC2 observations and other observations (HIRES and NIRSPAO) on EPIC 203868608 are summarized in Table 1.

The raw data were processed using a standard procedure, including replacing bad pixels, subtracting dark frames, flat fielding, and subtracting sky background. We constructed a bad pixel map using dark frames. Pixels with dark currents that deviated more than 5σ from their surrounding pixels were recorded as bad pixels. Their values were replaced with the median flux of the surrounding pixels. Dark frames were obtained with the exact same setting as the science frames, e.g., exposure time, coadds, and readout mode. After dark subtraction, each science frame was corrected for flat fielding. The reduced AO images (shown in Figure 1) were later used for photometric and astrometric measurements.

2.2. Keck/HIRES

We obtained high dispersion spectra for EPIC 203868608 using Keck/HIRES (Vogt et al. 1994) at 13 epochs between 2015 June and 2017 July. From the Keck/HIRES spectra we determined radial velocities (RVs) for the brighter components in

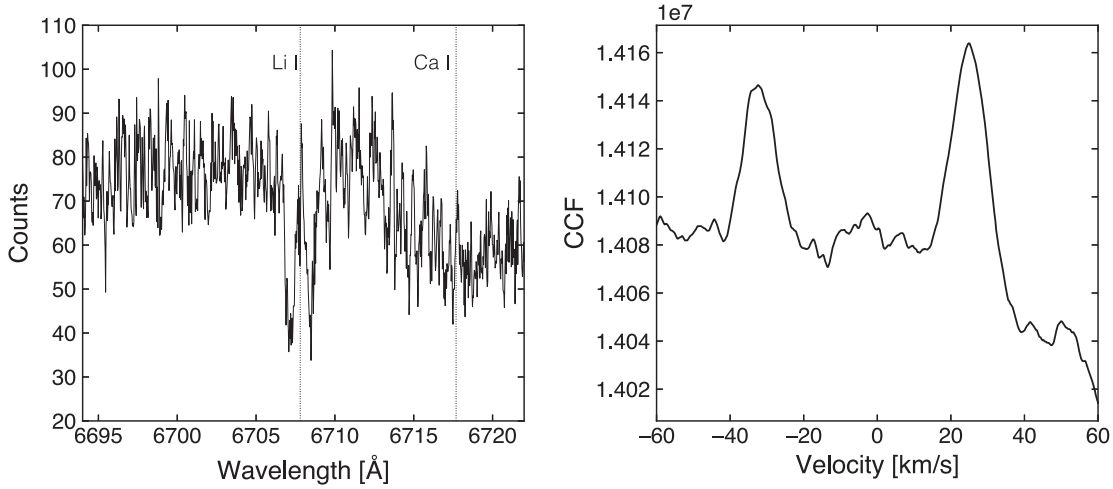

Figure 2. Left: a section of the HIRES spectrum for EPIC 203868608 at an epoch when the SB2 is near quadrature (2016 May 20). The Li I 6707.8 Å line is resolved for each component. The HIRES spectrum contains light from both the SB2 and EB, which are spatially unresolved. The EB component is too faint to contribute measurable features in HIRES spectra. Right: results of a cross-correlation of the spectrum left with another HIRES spectrum of EPIC 203868608 taken near conjunction of the SB2 orbit. Two peaks of the cross-correlation function are clearly visible, indicating two SB components.

the multiple stellar system. The majority of our data were acquired using the B2 or C5 deckers, which provide spectral resolution of 70,000 or 36,000, respectively, in the wavelength range of 4800–9200 Å. In this work, we also include previously published RVs derived from HIRES spectra acquired using the setup of the California Planet Search, covering ∼3600–8000 Å at $R \sim 48{,}000$ with the C2 decker. An example of HIRES spectra centering on the Li I 6707.8 Å line is given in Figure 2, showing the SB2 nature of EPIC 203868608 A. While some of the HIRES RVs are published in D16, the remainder will be presented in T. David et al. (2018, in preparation).

2.3. Keck/NIRSPAO

2.3.1. Instrument Setup

We observed EPIC 203868608 using Keck/NIRSPAO mode in the *K* band, for which the filter was "NIRSPEC-7-AO." We selected a slit with width of 0.″041 and length of 2.″26. The slit width corresponds to a 3 pixel sampling on the detector. The spectral resolution is ∼25,000 for the slit width.

2.3.2. Observation

We observed EPIC 203868608 on UT 2017 July 6, coinciding with the primary eclipse of the EB. We started to take data at UT 06:30 and finished taking data at UT 09:22. We used the "ABBA" dither pattern. Seeing was between 0.″8 and 1.″0. Wind speed was low between 0 and 5 mph.

Exposure time was set to be 600 s and 1 coadd per frame. The exposure was chosen to be short enough to resolve the eclipse duration (i.e., a few hours), and long enough for a decent signal to noise ratio (S/N). The peak flux recorded on the detector was ∼80–120 ADU (gain = $5.8\,e^{-1}$ per ADU), depending on-target airmass and seeing conditions.

We obtained four ABBA patterns corresponding to a total on-target time of 2.67 hr. Compared to the wall time duration of 2.87 hr, the observing duty cycle was 93%.

2.3.3. Reducing NIRSPAO Data

We reduced the NIRSPAO data with a python package PyNIRSPEC (Boogert et al. 2002; Piskorz et al. 2016). The procedure was as follows. Dark frames were subtracted from the raw images, which were then flat fielded. Bad pixels were identified in dark frames and their values were replaced by interpolating values of the surrounding pixels.

The raw images were then divided into different orders. Each order was processed independently, including the following procedures: rectification and wavelength calibration. The details of the data reduction can be found in Wang et al. (2017). The final data products of PyNIRSPEC are wavelength-calibrated and rectified 2D spectra.

We then extracted 1D spectra from the 2D spectra. The procedure was complicated for the EPIC 203868608 case: the two visual components were separated by 0.″126, which is $\sim 3\lambda/D$ in the *K* band. It is therefore expected that the extracted 1D spectrum of each visual component was contaminated by the other component. We describe our approach to minimize and remove the flux contamination as follows.

We created master spectra for A and B by stacking individual spectra over the course of observation. To minimize flux contamination, we only used the half of the point-spread function (PSF) that was away from the other component to extract the 1D spectrum. We used a two-component Moffat function to model the PSF. The master spectra for A and B were later used to remove flux contamination.

We then extracted 1D spectra at different epochs. The more points along the PSF that were used, the better the S/N. However, a larger contamination was incurred when more points along the PSF were used. We set quantitative criteria to decide which points to use for the 1D spectral extraction. First, the signal needed to be at least two times higher than the contamination. Second, the signal needed to be higher than 1/20 of the peak signal. The criteria ensured that the flux contamination was always smaller than 15% without significantly sacrificing incoming signal.

To further decrease the contamination level, we modeled the contamination and removed it from the extracted 1D spectrum.

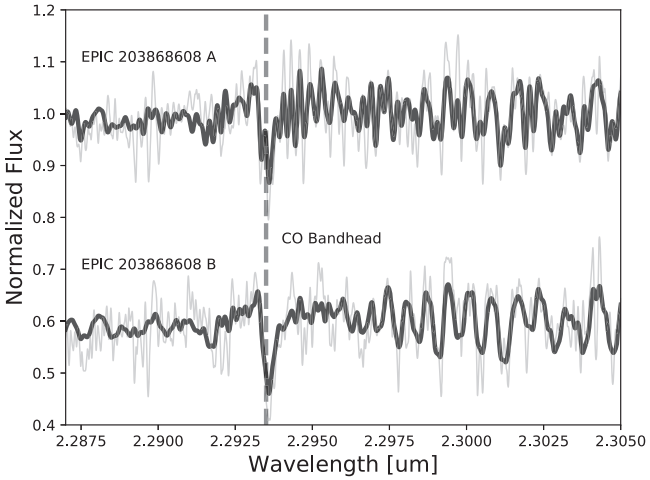

Figure 3. A section of NIRSPAO spectra for spatially resolved EPIC 203868608 A (top) and B (bottom) around a CO bandhead at 2.2935 μm. The two normalized spectra are offset for visual clarity. The CO bandhead is marked as a vertical dashed line. The gray lines are measured spectra, and the black lines are a synthetic spectrum convolving with kernels determined by least square deconvolution (Section 4.1). Two sets of spectra can be seen in the A spectrum, indicating the SB2 nature of EPIC 203868608 A.

The contaminating spectrum was obtained as the master spectrum for each component. The contamination level was calculated based on the two-component Moffat model. We integrated over the pixels that were used in the spectral extraction for the signal PSF and the contamination PSF. The ratio between the two integrals was the contamination level. We then removed the contamination from the single-epoch 1D spectrum.

For each visual component, we combined decontaminated spectra for each ABBA pattern, which resulted in spectra at four epochs. For the A and B dither positions, spectra were shifted along both the slit direction and the dispersion direction. Therefore, we shifted spectra so that they aligned in wavelength space. To do so, we cross-correlated spectra from the A and B detector positions, found the wavelength offset, and then aligned the spectra. An example of reduced spectra is given in Figure 3.

3. Results

3.1. Orbital Architecture

EPIC 203868608 is a quadruple system that consists of two binary systems separated by 0.″126 (A and B, see Figure 4). Aa and Ab compose a SB2. The orbit of component A is mapped using RVs from HIRES and NIRSPAO (Section 3.2). Ba and Bb compose an EB, whose orbital period is 4.54 days. The diluted light curve is measured by *K2* photometry and a solution for the orbital elements is presented in D16. The EB nature is also confirmed by Keck NIRC2 photometry measurements for in and out of the primary eclipse (Section 3.3). At a distance of 153 ± 7 pc (Gaia Collaboration et al. 2018), A and B have a projected separation of 19.3 au. This separation corresponds to an orbital period of more than 80 years, assuming a total mass of 1 solar mass for the quadruple system. Current astrometric data are not adequate to constrain the orbits for A and B. The fact that component A is not eclipsing in *K2* photometry indicates that the orbital planes of A and B are not strictly coplanar at the present time.

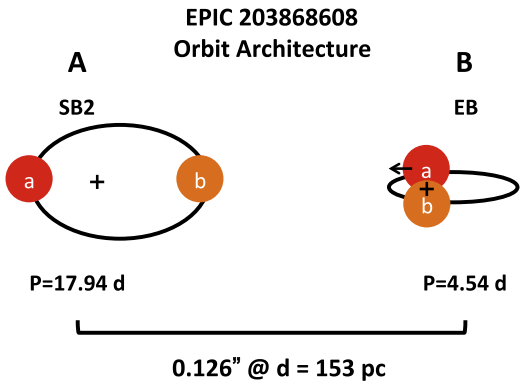

Figure 4. Illustration of orbit architecture for EPIC 203868608. The system consists of two visual components (A and B) that are separated by 0.″126. A is a spectroscopic binary on an eccentric orbit with a period of 17.94 days. The plus sign marks the focus of the ecliptic orbit. B is an EB with a period of 4.54 days. The arrow on the star a marks the rotational axis. See Table 2 for more information about the system.

3.2. RVs

RVs for the non-eclipsing SB2 were determined from the Keck/HIRES spectra via cross-correlation with RV standards using the FXCOR task in IRAF.[6] FXCOR uses the Tonry & Davis (1979) cross-correlation method and Gaussian or parabolic profiles to interactively fit for velocity shifts between the two components. We chose orders with high spectroscopic information content that exhibited the highest S/N and were relatively free of significant telluric contamination to determine the RVs. For each component, we used the error-weighted means of RV measurements from many individual orders as the final RV. Although the EB and the SB2 are near-equal brightness at NIR wavelengths and both are within the HIRES slit at each epoch, we detected only two clear peaks in the cross-correlation function (CCF). This is likely due to large $v \sin i$ and a fainter magnitude in the optical wavelengths for the EB. The values of the HIRES RVs will be presented in T. David et al. (2018, in preparation).

With the JKTEBOP software we performed joint fits to the RV time series in order to determine the orbital and physical parameters of the SB2. We present these parameters in Table 3, where the uncertainties were determined from 10,000 Monte Carlo simulations. We show fits to the RV time series in Figure 5. We find a minimum system mass of $(M_{Aa} + M_{Ab})\sin^3 i = 0.3685 \pm 0.0050\, M_\odot$. If one assumes the expected value of $\langle \sin^3 i \rangle = 3\pi/16$, this translates to a system mass of $(M_{Aa} + M_{Ab}) \sim 0.63\, M_\odot$. Further details on the modeling of the RVs can be found in T. David et al. (2018, in preparation), which supersedes the D16 work that was based on the assumption (now realized as erroneous) that the EB and the SB2 period were the same, rather than arising from two different orbit signals.

3.3. Photometry and Astrometry

We measured differential photometry for the two visual components in EPIC 203868608 using a customized code. During the primary eclipse, ΔJ and ΔK_P were 0.44 ± 0.04 and 0.58 ± 0.01. In another epoch, out of an eclipse, ΔJ and ΔK_P

[6] IRAF is distributed by the National Optical Astronomy Observatory, which is operated by the Association of Universities for Research in Astronomy (AURA) under a cooperative agreement with the National Science Foundation.

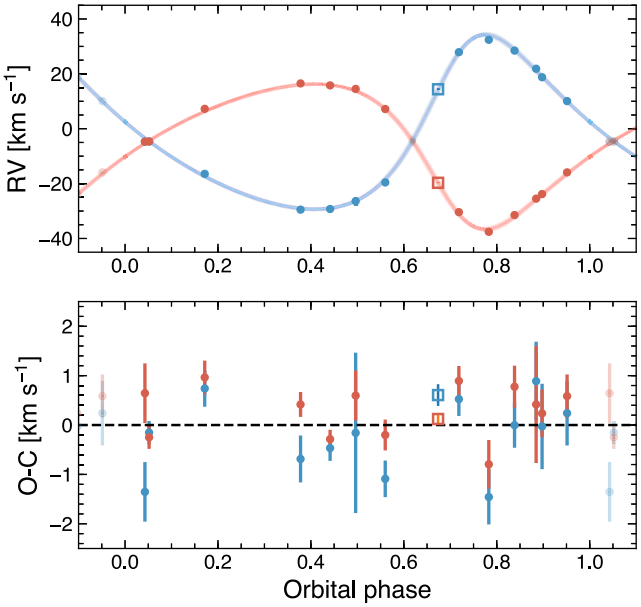

Figure 5. Joint fits to the RV time series of the spectroscopic binary component of EPIC 203868608. The filled circles represent HIRES measurements while the open squares indicate the NIRSPAO measurements.

were 0.23 ± 0.01 and 0.28 ± 0.01. We used a photometric aperture of 6 pixels to measure the flux for A and B. We used an annulus with a radius of 60 pixels and width of 20 pixels to estimate the background. The measurement uncertainty was calculated using the standard deviation of measurements for different individual frames. The differential photometry measurement indicates that the fainter visual component (component B) is responsible for the eclipses observed in K2 photometry and presented in D16.

Astrometric measurements were also conducted with a customized code, in which stellar PSFs were fitted by a 2D Gaussian function. The centroids of the fits were used to calculate angular separation and position angle between A and B. We used a pixel plate scale of 9.952 mas (Yelda et al. 2010). The measurements were consistent between the two epochs and between the two filters. The angular separation between A and B is $0\farcs126 \pm 0\farcs004$. The position of the angle of B with respect to A is $-80\fdg99 \pm 0\fdg10$ (see also Table 2).

3.4. System Masses

From the out-of-eclipse contrasts in the J and K_P bands and the Baraffe et al. (2015) models, we calculated plausible system masses for the EB given a range of assumed system masses for the SB2 (Figure 6). In this analysis we assumed for simplicity that both components of the SB2 are equal in mass, and both components of the EB are equal in mass. We assumed an age of 8 Myr, though this analysis is fairly insensitive to the choice of age between 5 and 10 Myr. Solutions in which the SB2 are less than the minimum mass measured from orbit-fitting could be excluded. We also considered solutions in which the total mass of the SB2 is greater than the total mass of the binary UScoCTIO 5 (total mass of 0.65 $M_\odot$, Kraus et al. 2015; David et al. 2016) to be highly unlikely. This is because EPIC 203868608 clearly resides at a fainter and redder position in the color–absolute magnitude diagram with respect to UScoCTIO 5, which has only two components despite sharing a similar spectral type. We thus considered the most plausible mass range for the SB2 to be $\sim$0.4–0.6 $M_\odot$, corresponding to a range of $\sim$0.3–0.5 $M_\odot$ for the EB.

Due to the fact that only the SB2 is detected in our Keck/HIRES spectra, we cannot presently measure fundamental masses and radii for the EB. Future efforts using either high-resolution IR spectroscopy or spatially resolved spectroscopy at a range of phases should allow for the determination of masses and radii (A. Kraus 2018, private communication). Moreover, long-term astrometric monitoring via high-resolution imaging should enable the determination of the wide EB+SB2 orbit. At that point, it should be possible to determine dynamical masses for each of the four components in the system and begin to place stringent constraints on evolutionary models for low-mass stars (e.g., Mathieu 1994; Hillenbrand & White 2004; Mathieu et al. 2007; Stassun et al. 2014).

3.5. Comparing EPIC 203868608 to Other Quadruple Systems

The orbital architecture of EPIC 203868608 is typical of other known quadruple systems, which regularly show four stars with similar masses and similar periods of the inner subsystems (Tokovinin 2008). The ϵ Lyr system (composed of four A-type stars) is considered a prototype of this type of quadruple architecture, and BD -22 5866 (Shkolnik et al. 2008) is an example at masses similar to those in the EPIC 203868608 system. One proposed formation channel for such hierarchical quadruples is through cascade fragmentation, in which a rotating core collapses into a centrifugally supported disk, which then undergoes further rotational fragmentation if the angular momentum of fragments in the disk is high enough (Bodenheimer 1978). N-body dynamics between fragments within a pre-stellar core is another proposed mechanism for the origin of such 2+2 quadruples or "double twins," although such an outcome is rare with this mechanism (Delgado-Donate et al. 2004). Assuming an outer period of 80 years, the location of EPIC 203868608 in a $P_{\rm in}$–$P_{\rm out}$ diagram, where $P_{\rm in}$ is the period of either of the inner subsystems (comparable in this case), is indeed quite close to the region of highest density among known quadruple systems (see Figure 11 of Tokovinin 2008). This observation would seem to suggest that whatever mechanism is responsible for creating such systems would need to act on timescales much shorter than that of the age of EPIC 203868608 ($\lesssim$10 Myr).

EPIC 203868608 joins a relatively small list of pre-main-sequence (PMS) quadruple systems which, if characterized well, can place tight constraints on evolutionary models and formation scenarios. Other notable PMS quadruples include GG Tau (White et al. 1999), V773 Tau (Boden et al. 2007), LkCa 3 (Torres et al. 2013), and 2M0441+2301 (Bowler & Hillenbrand 2015).

4. EB Obliquity

Obliquity is defined as the angle between the rotational axis of the eclipsed star and the orbital angular momentum vector of the eclipsing system. The obliquity for an EB system can be measured via the Rossiter–McLaughlin (RM) effect (McLaughlin 1924; Rossiter 1924) or, more generally, through spectral line profile (LP) changes during an eclipse, i.e., Doppler tomography.

For a fast-rotating object, the spectral LP is mainly broadened by the rotation. During an eclipse, the spectral LP would deform because certain velocities are missing due

Table 2
Photometry, Astrometry, and Orbital and Physical Parameters of EPIC 203868608

Parameter	Units	Value	
		AB	
Distance	pc	153 ± 7[a]	
J	mag	11.86[b]	
H	mag	11.14[b]	
K_s	mag	10.76[b]	
ΔJ	mag	0.23 ± 0.01	
ΔK_p	mag	0.28 ± 0.01	
Angular separation, ρ	arcsec	0.126 ± 0.004	
Position angle	degree	−80.99 ± 0.10	
		Aab	Bab
Period, P	days	17.9420 ± 0.0012	4.541710 ± 0.000019[c]
Eccentricity, e	⋯	0.2998 ± 0.0041	0.3224 ± 0.0042[c]
Epoch, T_o	BJD	2457175.182 ± 0.031	2456896.19699 ± 0.00019[c]
Longitude of periastron, ω	degree	316.36 ± 0.93	100[d]
Semimajor axis, a	au	0.09616 ± 0.00044	0.0359[d]
Minimum system mass, $(M_1 + M_2)\sin^3 i$	$M_\odot$	0.3685 ± 0.0050	0.3[d]
Mass ratio, q	⋯	0.8309 ± 0.0062	1.0[d]
Obliquity, λ	degree	⋯	-57^{+40}_{-36}

Notes.
[a] Gaia Collaboration et al. (2018).
[b] Cutri et al. (2003).
[c] David et al. (2016).
[d] Guessed values used in obliquity measurement (Section 4).

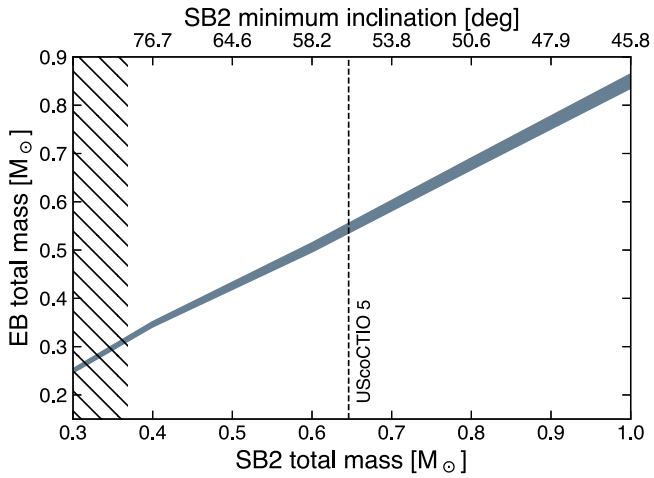

Figure 6. Plausible masses for the spectroscopic binary EPIC 203868608 A and the EB EPIC 203868608 B based on BHAC15 models and the J- and K_P-band contrasts, indicated by the narrow diagonal shaded band. The left-most region (hatched region) of the parameter space is excluded by the minimum mass of the SB2. The vertical dashed line indicates the total mass of the young binary UScoCTIO 5, which has a similar primary spectral type and is a binary with well-determined parameters. We consider solutions to the right of this line to be highly unlikely for the now-appreciated quadruple star system, but cannot rule them out.

to the occultation. As the eclipse progresses, the spectral LP deformation exhibits certain patterns for a given obliquity. For example, the spectral LP would redshift and then blueshift for a prograde orbit and vice versa. In subsequent subsections, we will describe the procedure to measure LPs during an eclipse (Section 4.1), model LPs (Section 4.3), and infer the EB obliquity from the LP measurement and modeling (Section 4.4).

Table 3
Parameters of the EPIC 203868608 Aab Spectroscopic Binary

Parameter	Units	Value
Directly measured parameters		
Orbital period, P	days	17.9420 ± 0.0012
Epoch, T_0	BJD	2457175.182 ± 0.031
Primary Doppler semi-amplitude, K_1	km s^{-1}	26.46 ± 0.16
Secondary Doppler semi-amplitude, K_2	km s^{-1}	31.84 ± 0.18
Systemic RV, γ	km s^{-1}	−4.436 ± 0.072
Eccentricity, e		0.2998 ± 0.0041
Longitude of periastron, ω	degree	316.36 ± 0.93
rms of primary RV fit	km s^{-1}	0.6
rms of secondary RV fit	km s^{-1}	0.8
$\chi^2_{\rm red}$ of primary RV fit		2.2
$\chi^2_{\rm red}$ of secondary RV fit		2.7
Derived parameters		
Mass ratio, q		0.8309 ± 0.0062
Minimum system mass, $(M_1 + M_2)\sin^3 i$	$M_\odot$	0.3685 ± 0.0050
Orbital separation, a	au	0.09616 ± 0.00044

4.1. LP Measurement

We derived the LP using the least square deconvolution method. The method is detailed in Wang et al. (2017) and can be summarized by the following equation:

$$\boldsymbol{Z} = (\boldsymbol{M}^T \cdot \boldsymbol{S}^2 \cdot \boldsymbol{M} + \boldsymbol{R})^{-1} \cdot \boldsymbol{M}^T \cdot \boldsymbol{S}^2 \cdot \boldsymbol{Y}^0, \quad (1)$$

where matrix transpose is denoted by $\boldsymbol{T}$, $\boldsymbol{Z}$ is the LP, $\boldsymbol{M}$ is a $m \times n$ Toeplitz matrix, where m is the number of data points in a spectrum and n is the desired number of data points in the LP. $\boldsymbol{M}$ is generated from a template spectrum $\boldsymbol{F}$ that has the same wavelength sampling as the observed spectrum $\boldsymbol{Y}^0$. $\boldsymbol{S}$ is an

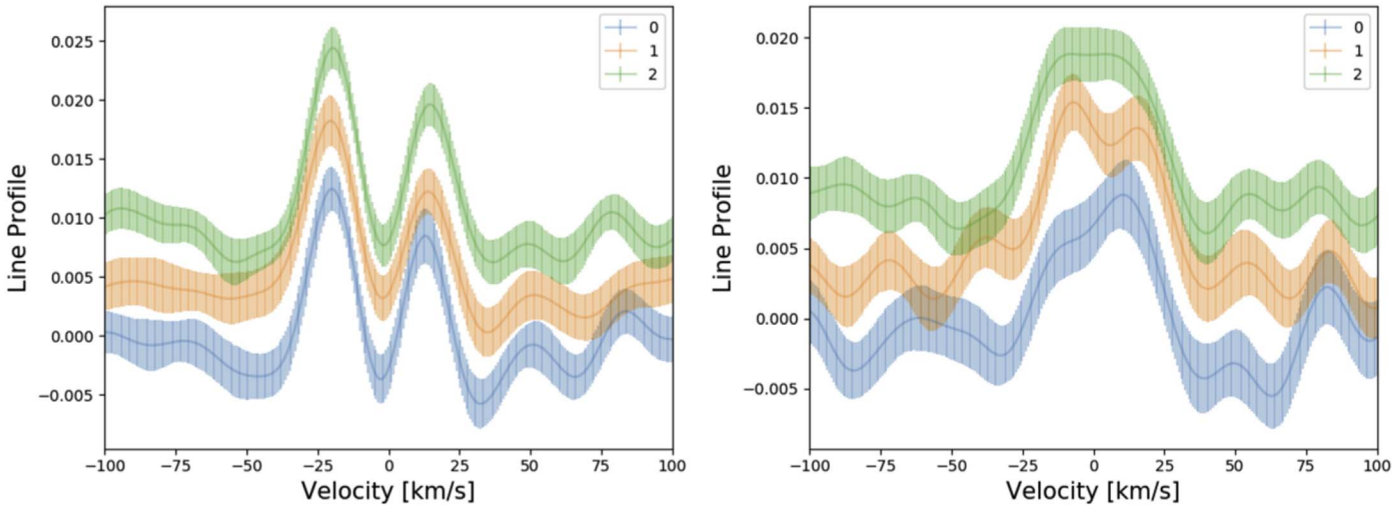

Figure 7. Left: LPs for EPIC 203868608 A at three epochs of NIRSPAO observations. Velocity shift of LPs are corrected for instrument drift (using telluric lines) and barycentric velocity. Right: the same as the left but for EPIC 203868608 B. The colors and numbers represent epochs in NIRSPAO observations: 0, mid-eclipse; 1, egress; and 2, out of eclipse.

$m \times m$ matrix with $\boldsymbol{S}_{ii} = 1/\sigma_i$, where σ_i is the measurement error for each spectral data point. We use PHOENIX BT-Settl spectrum (Allard et al. 2001) with $T_{\rm eff} = 2900$ K and $\log(g) = 4.0$ as our template spectrum $\boldsymbol{F}$. The spectrum gives the least residual in the least square deconvolution.

$\boldsymbol{R}$ is a regularization matrix. We used a first-order Tikhonov matrix as the regularization matrix in Wang et al. (2017). Here, we use the inverse of a covariance matrix as the regularization matrix. We denote the covariance matrix as $\boldsymbol{K}(\alpha_Z)$, where α_Z is a set of parameters. The covariance matrix can have many forms, but we adopt a commonly used form—the squared exponential covariance matrix:

$$K_{ij}(\sigma_Z, \lambda_Z) = \sigma_Z^2 \exp\left[-\frac{(v_i - v_j)^2}{2\lambda_Z}\right], \quad (2)$$

where v_i is the corresponding velocity for an LP.

There is an advantage to replacing the first-order Tikhonov matrix with an inverse covariance matrix: $\boldsymbol{Z}$ is a multivariate Gaussian distribution that can be calculated in the Bayesian framework (Asensio Ramos & Petit 2015):

$$\boldsymbol{Z} = \mathbb{N}(\boldsymbol{\mu_Z}, \boldsymbol{\Sigma_Z}), \quad (3)$$

where $\mathbb{N}$ denotes a multivariate Gaussian distribution, $\boldsymbol{\mu_Z}$ and $\boldsymbol{\Sigma_Z}$ are the mean and covariance matrix for the multivariate Gaussian distribution. $\boldsymbol{\Sigma_Z}$ and $\boldsymbol{\mu_Z}$ can be calculated using the following two equations as derived from Asensio Ramos & Petit (2015):

$$\boldsymbol{\Sigma_Z} = [\boldsymbol{M}^T \cdot \boldsymbol{S}^2 \cdot \boldsymbol{M} + \boldsymbol{K}(\hat{\alpha}_Z)^{-1}]^{-1}, \quad (4)$$

where $\hat{\alpha}_Z$ is the set of parameter that maximizes the marginal posterior for α_Z. Assuming the distribution of α_Z is strongly peaked, we can follow the Type-II maximum likelihood solution (Bishop 1995) for $\boldsymbol{\Sigma_Z}$ and $\boldsymbol{\mu_Z}$. With $\boldsymbol{\Sigma_Z}$ calculated, $\boldsymbol{\mu_Z}$ can be calculated using the following equation:

$$\boldsymbol{\mu_Z} = \boldsymbol{\Sigma_Z} \cdot \boldsymbol{M}^T \cdot \boldsymbol{S}^2 \cdot \boldsymbol{Y}^0. \quad (5)$$

Figure 7 shows LPs for A and B based on NIRSPAO observations. Three epochs are shown for mid-eclipse (−0.08 hr), egress (0.67 hr), and out of eclipse (1.32 hr). The times in parentheses indicate elapsing time with respect to the center of the primary eclipse (at 0.0 hr) for an eclipse that lasts for 2.7 hr. Note that we combine the last two epochs of NIRSPAO observations to increase the S/N for the out-of-eclipse LP.

4.2. RVs for EPIC 203868608 A and B Derived from an LP

Owing to the AO system that spatially separates the two visual components, we can measure RVs for individual components using the following equation: $v = \bar{v} - v_{\rm atm} + {\rm bcc}$, where $\bar{v}$ is the velocity center of the measured LP, $v_{\rm atm}$ is the velocity center of the measured LP for telluric lines, and bcc is the barycentric correction (Wright & Eastman 2014). We use two methods to calculate the velocity center of an LP: measuring the flux-weighted centroid and polynomial fitting for the LP peak. Both methods yield consistent results. The RV value and uncertainty are estimated by repeating the RV measurement for 100 iterations. In each iteration, correlated Gaussian noise is added to the LP. We report the average and the standard deviation as the RV value and its uncertainty.

The RVs for Aa and Ab are $14.39 \pm 0.22\,{\rm km\,s^{-1}}$ and $-19.71 \pm 0.12\,{\rm km\,s^{-1}}$, respectively. These are consistent with the orbital solution found from the HIRES RV measurements (see Figure 5). We do not resolve the RV difference between Ba and Bb because the observation was taken when Ba and Bb were eclipsing and ΔRV should be around zero. Instead, we measure the systemic RV for B, which is $0.38 \pm 0.69\,{\rm km\,s^{-1}}$.

The offset of systemic RV between A ($-4.44 \pm 0.07\,{\rm km\,s^{-1}}$) and B ($0.38 \pm 0.69\,{\rm km\,s^{-1}}$) is significant at the 6-σ level. This casts doubt on the physical association between A and B, although both velocities are within $\sim 2\sigma$ of the median RV for the Upper Sco association as a whole (Gaia Collaboration et al. 2018). However, the discrepancy may be reconciled by the following counter arguments. First, the orbital motion of B around A could account for up to $\sim 3\,{\rm km\,s^{-1}}$ (i.e., a majority of the discrepancy), assuming a total mass of $0.8\,M_\odot$ and a separation of 20 au. Second, the angular separation of $0\farcs126$ makes it unlikely to have an equal-brightness optical double that is physically unassociated (Horch et al. 2014).

4.3. LP Modeling

We adopt an analytic solution to model LPs for an EB (J. M. Pezzato et al., 2018 in preparation). The analytic model greatly reduces the computational time compared to finite-element models that are usually used for EB LP analysis (e.g., Albrecht et al. 2007; Johnson et al. 2014). Our approach is similar to the analytic method to model the RM effect for transiting planets (Hirano et al. 2011). The deformed LP during transit is the out-of-transit LP minus a "Doppler shadow," which is the line spread function (LSF) of the spectrograph centered at the blocked velocity and scaled by the flux blocked by the planet. The differences are (1) the occulting object can no longer be treated as a point source and (2) the occulting object is self-luminous in the EB case rather than a dark spot in the planet case.

To address the point source problem, we calculate the maximum and minimum velocity of the occulted area, and construct a rotationally broadened LP based on the two velocities. The LP is then convolved with the LSF of the spectrograph, which is measured using telluric lines at low airmass.

The self-luminous problem is addressed by adding another LP that is from the occulting star and that is scaled by the relative flux between the secondary and the primary star. Therefore, the final LP is the unocculted LP of the primary, minus the flux-scaled occulted LP, and plus the flux-scaled LP of the secondary, and then normalized so that the total area under the curve equals to unity. The reader is referred to Appendix B for a comparison between the analytic model and a finite-element model (Albrecht et al. 2014, and references therein).

The parameters in our analytic model are impact parameter, obliquity, eclipse duration (2.7 hr), $v \sin i$ for the primary and secondary stars, radius ratio between the primary and the secondary (1.0), orbital period (4.54 days), total mass ($0.3\,M_{\odot}$) and mass ratio (0.8), flux ratio (0.8), quadratic limb darkening parameters (0.8 and 0.1) (Claret et al. 2012), eccentricity (0.3), argument of periastron (100°), time at periastron (2456896.19699 BJD), and a y-axis scaling factor for the LPs. The parameters with values indicated in parentheses are fixed in the following inference for obliquity because they are either well constrained by observations (e.g., D16) or variation of the parameters does not significantly change the obliquity measurement.

4.4. Results for Obliquity Measurement

We generate posterior samples for the LP parameters by exploring the likelihood space of model fits to the data using an affine-invariant Markov chain Monte Carlo (MCMC, Goodman & Weare 2010) as implemented in the Python package EMCEE (Foreman-Mackey et al. 2013). We include the following parameters in the MCMC: impact parameter (b), obliquity (λ), and $v \sin i$ for the primary and the secondary star. We apply uniform priors to these parameters within their boundaries, $0 < b < 1$, $-180° < \lambda < 180°$, and $0 < v \sin i < 50\,\mathrm{km\,s^{-1}}$. Convergence criteria include: (1) the length of MCMC chains is at least 100 times autocorrelation length and (2) the change of the autocorrelation length estimates between consecutive check are less than 5%. The chain was considered converged when both of these criteria were met for each freely fitted parameter. Figure 8 shows the posterior distribution. Median values and uncertainties for different parameters are $b = 0.36^{+0.49}_{-0.26}$, $\lambda = -57^{+40}_{-36}$ degrees, $V \sin i_1 = 31.2^{+3.1}_{-3.0}\,\mathrm{km\,s^{-1}}$, $V \sin i_2 = 29.6^{+2.4}_{-2.2}\,\mathrm{km\,s^{-1}}$, and the y-axis scaling factor $= 1.16^{+0.05}_{-0.05}$. The uncertainties are calculated by subtracting 68% interval by the median values. Figure 9 shows LPs that are drawn from the posterior samples in comparison with LP measurements at different epochs.

Posterior distribution of obliquity λ shows a clearly multi-modal distribution. While the posterior number density is low, there is an island of positive obliquity values. These represent cases in which the secondary transverses the opposite side of the primary equator with the same impact parameter b. On the island of negative obliquity values where the number density is the highest, there appears to be a bimodal distribution. However, the lower-obliquity peak around 20° is correlated with higher value of b, which are cases for grazing eclipse. This situation is unlikely given the low value of b as inferred from light curve fitting (David et al. 2016). Therefore, a careful examination of the multimodal distribution of posterior distribution of obliquity further favors an orbit with high obliquity.

The large uncertainty in obliquity is due to the following reasons: (1), data quality is not high because of challenging AO-aided high-resolution spectroscopy; (2), we do not have a complete coverage of the eclipse, only data points during the eclipse are taken; (3), we have incomplete knowledge on the orbital parameters; and (4) correlated noise in the observations is not well understood. The reader is referred to Appendix A for a discussion on the sensitivity of our NIRSPAO observations to the RM effect from EPIC 203868608.

4.5. Implications of an Inclined Orbit

Doppler tomography data suggest that EPIC 203868608 Bb is on an inclined orbit around Ba with an obliquity of -57^{+40}_{-36} degree with a 2-σ upper limit at $-2\overset{\circ}{.}9$.

The inclined orbit has significant implications for the stellar properties of low-mass stars and the formation history of the quadruple system. Specifically, the high obliquity puts constraints on the tidal quality factor Q and the mechanism through which EPIC 203868608 forms.

4.5.1. Tidal Quality Factor

EPIC 203868608 is young and both components have eccentric orbits. This indicates that the tidal circularization timescale should be longer than the system age (~10 Myr). Here we use that fact to constrain the tidal quality factor for the low-mass stars in EPIC 203868608. Since constraints are stronger for systems with shorter periods, we will discuss the EB component, the period of which ($P = 4.54$ days) is shorter than that for the SB2 ($P = 17.94$ days). The rate at which eccentricity changes due to tidal dissipation is given as follows (Hut 1981):

$$\dot{e} = 27\frac{k}{T}q(1+q)\left(\frac{R}{a}\right)^3 \frac{e}{(1-e^2)^{13/2}} \times \left(f_3(e^2) - \frac{11}{18}(1-e^2)^{3/2} f_4(e^2)\frac{\Omega}{n}\right), \quad (6)$$

where $k = 0.28$, which is twice the Love number (Batygin & Adams 2013); q is the mass ratio, which is assumed to unity here; R/a is the ratio of the radius of the primary star to the semimajor axis, which is constrained by light curve fitting in D16: $R/a = 0.0679$; $e = 0.3227$ is eccentricity (D16). The

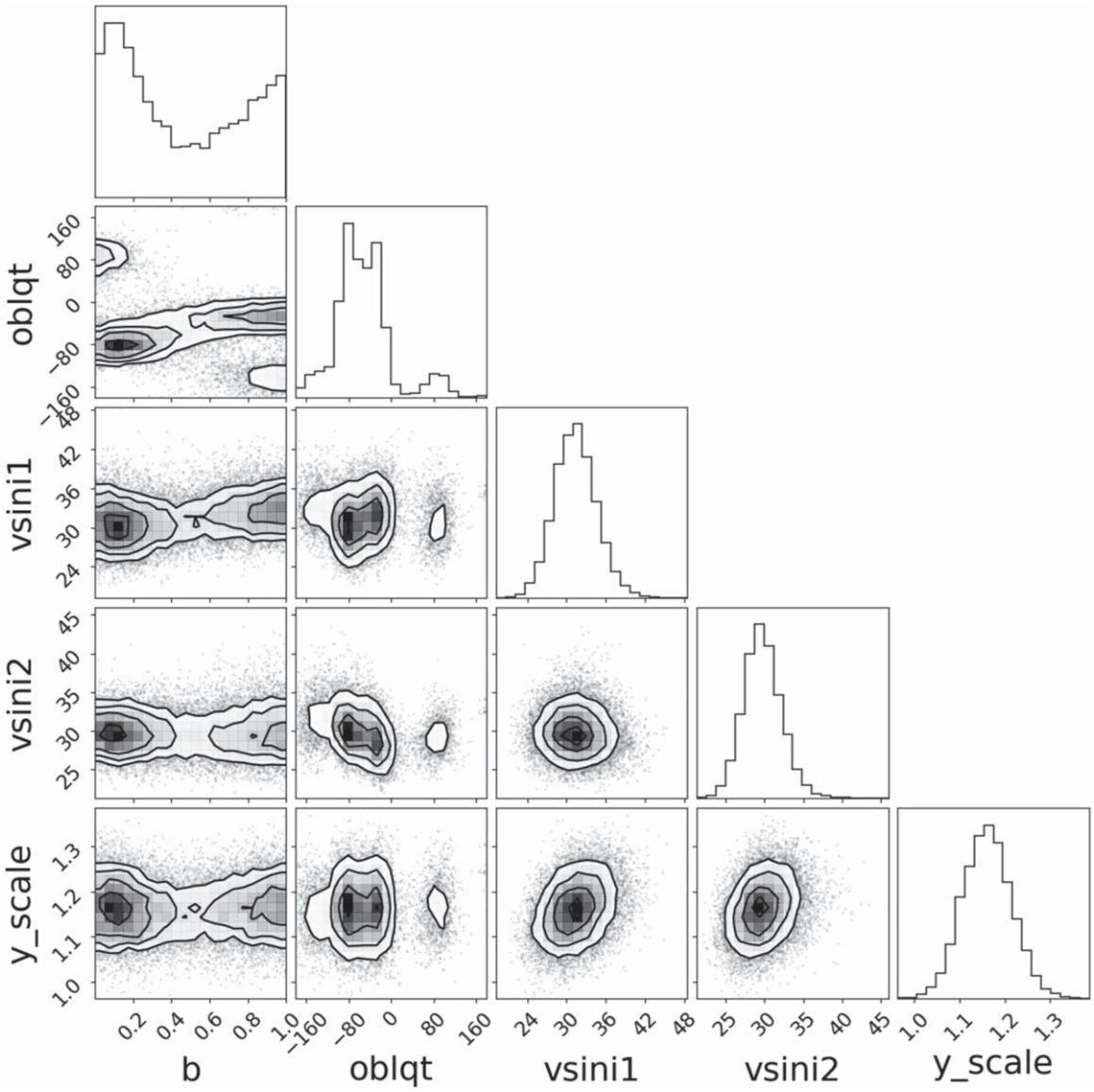

Figure 8. Posterior sample distributions for parameters in modeling LP variation during the eclipse of EPIC 203868608 Bab.

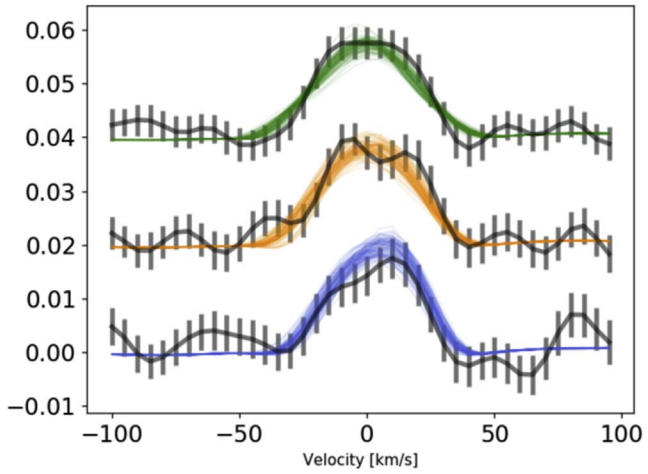

Figure 9. LPs at three epochs: mid-eclipse, egress, and out of eclipse. The gray points linked by solid gray lines are LP measurements for EPIC 203868608 Bab (the same as Figure 7 right). The solid colored lines are random draws from MCMC posterior samples.

expression of f_3 and f_e can be found in Hut (1981). Ω and n are the angular velocities of the rotation and orbit: Ω is inferred from $v \sin i$ measurement and n is inferred from orbital parameters from light curve fitting in D16. T in Equation (6) is:

$$T = \frac{R^3}{GM\tau}, \tag{7}$$

where τ is the inverse of the product of the tidal quality factor Q and n (Peale 1999).

Next, the tidal circularization timescale $\tau_{\rm circ}$ can be calculated as $e/\dot{e}$. In order for $\tau_{\rm circ}$ to be longer than 10 Myr, Q needs to be higher than 5×10^4. This finding is consistent with previous works on tidal Q (e.g., Matsumura et al. 2008).

Additional constraints on tidal Q can be obtained from the inclined orbit, which suggests that the synchronization process is not finished. To synchronize the rotational and orbital period, the system needs to be aligned in the first place. Therefore, the age of the system should be smaller than the tidal synchronization timescale, which can be estimated using the following

equation (Rasio et al. 1996):

$$\tau_{\rm sync} \approx Q \cdot \omega \cdot q\left(\frac{R_2^3}{Gm_2}\right)\left(\frac{a}{R_2}\right)^6, \quad (8)$$

where ω is the difference of angular frequency between the primary rotation and orbit, and R_2 is the radius of the secondary star. Given that $\tau_{\rm sync} > 10$ Myr, Q needs to be higher than 5×10^5. Note that the constraint from tidal synchronization is 10 times stronger than that from tidal circularization. Nonetheless, the allowed range for the tidal quality factor ($Q > 5 \times 10^5$) is still consistent with previous studies.

4.5.2. Kozai–Lidov (KL) Perturbation versus Stochastic Processes

We investigate here if the EB was formed through KL perturbations (Kozai 1962; Lidov 1962). KL perturbations are known to result in highly inclined orbit for exoplanets (e.g., HD 80606, Pont et al. 2009). In order for the KL mechanism to operate, the KL timescale needs to be shorter than the general relativity (GR) precession timescale. The KL timescale can be calculated using the following equation (Fabrycky & Tremaine 2007):

$$\tau_{\rm KL} = \frac{2P_{\rm out}^2}{3\pi P_{\rm in}}\frac{m_1+m_2+m_3}{m_3}(1-e_{\rm out}^2)^{3/2}, \quad (9)$$

where P is the orbital period, subscripts in and out denote the EB and the perturber, m is mass, subscripts 1, 2, and 3 denote primary and secondary in the EB, and the perturber, and e is eccentricity.

The GR precession timescale can be calculated using the following equation (Fabrycky & Tremaine 2007):

$$\tau_{\rm GR} = \frac{2\pi c^2}{3{\rm G}^{3/2}}\frac{a_{\rm in}^{5/2}}{(m_1+m_2)^{3/2}}(1-e_{\rm in}^2), \quad (10)$$

where c is the speed of light, G is the gravitational constant, $a_{\rm in}$ is the semimajor axis for the EB, and $e_{\rm in}$ is the eccentricity for the EB.

Assuming $P_{\rm in} = 4.54$ days, $P_{\rm in} = 88.6$ years, $m_1 = 0.15\,M_\odot$, $m_2 = 0.15\,M_\odot$, $m_3 = 0.4\,M_\odot$, $a_{\rm in} = 0.0359$ au, and $e_{\rm in} = 0.32$, the condition that $\tau_{\rm KL} < \tau_{\rm GR}$ is $e_{\rm out} > 0.82$. However, one needs to note that $\tau_{\rm GR}$ is a strong function of $a_{\rm in}$. Tracing back in time when $a_{\rm in}$ was larger, $\tau_{\rm GR}$ can be longer than $\tau_{\rm KL}$, and the requirement for $e_{\rm out}$ is relaxed to lower values.

Alternatively, the orbital architecture of EPIC 203868608 may be an evolutionary consequence of an even higher-order multiple star system (Ghez et al. 1993). It is shown in numerical simulations that hierarchical multiples can result from dynamical interactions of young stellar multiples formed by fragmenting cloud (Sterzik & Durisen 1998). Spin–orbit misalignment may take place during this formation stage. In addition, star–disk interaction in a multiple star system can also lead to spin–orbit misalignment (Spalding & Batygin 2014).

5. Summary and Discussion

We provide observational evidence that EPIC 203868608 is a quadruple stellar system in the Upper Scorpius OB association. The system consists of two visual components, one being an SB2 and the other being an EB. All stellar components are consistent with being young low-mass stars (age ~10 Myr and individual masses lower than ~0.3 $M_\odot$) that are still undergoing PMS contraction.

Our observations include: Keck NIRC2 observations that spatially separates the two visual components and confirms the west component as the EB (Section 3.3); Keck HIRES observations that constrains the total mass and eccentricity for the SB2 and therefore the total mass of the system (Section 3.4); Keck NIRSPAO observations that indicates an inclined orbit for the EB (Section 4). The system represents a rare opportunity to test theories on star formation and subsequent dynamical evolution (Section 4.5).

We place a cautionary note here. The NIRSPAO observation is very challenging: namely, to spatially separate a 0.″126 binary and measure LP changes for faint low-mass stars. As a result, only three data points have been taken, out of which an inclined orbit of EPIC 203868608 B is inferred. Future AO-aided high-resolution spectroscopy observations are necessary to confirm this result. Available instruments include but are not limited to the upgraded NIRSPEC (Martin et al. 2014), CRIRES+ (Follert et al. 2014), the infrared Doppler instrument (Kotani et al. 2014), and the Keck Planet Imager and Characterizer (Mawet et al. 2016).

We develop a framework to infer orbital obliquity for eclipsing systems such as transiting planets and eclipsing stars. The framework includes an analytic approach to model LPs during an eclipse (Section 4.3). Unlike previous analytic models, the analytic model can properly handle spectrally resolved and/or self-luminous occulters, which is essential to modeling EBs and large planets around small stars. Additionally, the framework includes a matrix-based method to retrieve LPs and their uncertainties from high-resolution spectroscopic data (Section 4.1). Together, the framework offers an efficient way of inferring obliquity (Section 4.4) and conducting simulations to check the robustness of the inference (Appendix A).

The framework will be particularly useful in studying the orbital architecture of eclipsing systems in the era of *Kepler* and *TESS* when numerous transiting planets and EB systems are being and will be discovered.

We thank the anonymous referee for his or her comments and suggestions that significantly improved the manuscript. We acknowledge Konstantin Batygin, Jim Fuller, and Fred Adams for discussions on tidal evolution and Kozai–Lidov perturbation in EPIC 203868608. We thank the PIs of KOA NIRC2 data, Christoph Baranec and Andrew Mann. S.A. acknowledges the support of the Danish Council for Independent Research, through DFF Sapere Aude Starting Grant No. 4181-00487B. Funding for the Stellar Astrophysics Centre is provided by The Danish National Research Foundation (Grant Agreement No. DNRF106). Part of this research was carried out at the Jet Propulsion Laboratory, California Institute of Technology, under a contract with the National Aeronautics and Space Administration. T.J.D. acknowledges support from the JPL Exoplanetary Science Initiative. The data presented herein were obtained at the W. M. Keck Observatory, which is operated as a scientific partnership among the California Institute of Technology, the University of California, and the National Aeronautics and Space Administration. The Observatory was made possible by the generous financial support of the W. M. Keck Foundation. The authors wish to recognize and acknowledge the very significant cultural role and reverence that the summit of Maunakea has always had within the indigenous Hawaiian community. We are most fortunate to have the opportunity to conduct observations from this mountain.

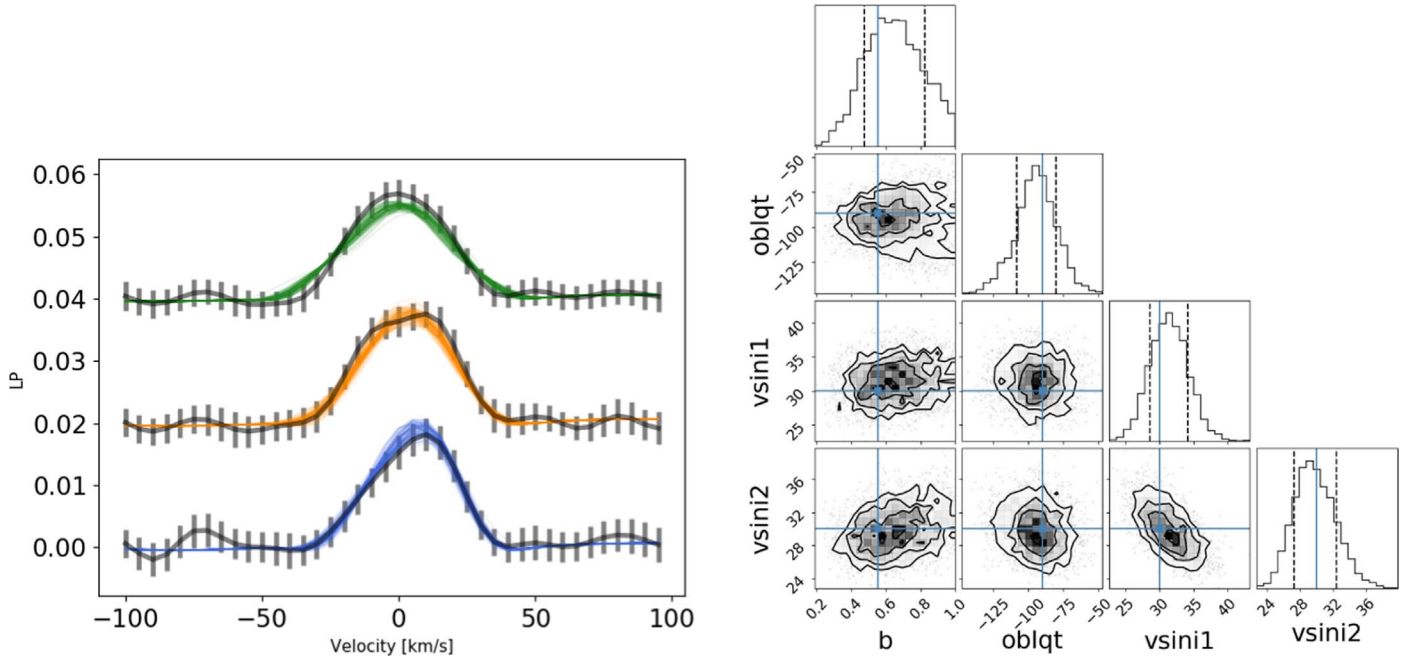

Figure 10. Left: LPs at different epochs for mocked data with an obliquity of −90°. The gray data points with errorbars are mocked data. The colored lines are random draws from posterior distributions. Right: posterior distribution of model parameters. The dashed lines mark the 16 and 84 percentiles. The blue lines mark the input values.

Appendix A
Sensitivity of NIRSPAO Observations to the RM Effect

We investigate if we can robustly measure the obliquity and how well we can retrieve the information in the presence of noise. In order to answer the two questions, we run simulations to (1) generate LPs that are affected by the RM effect; (2) generate mocked observational data based on the LPs and with realistic noise; and (3) use the same package as described in Section 4 to analyze the mocked data.

We consider a polar orbit with an obliquity of −90°. We use the same model as described in Section 4.3 to model LPs. All the parameters in the model are the same as the measured ones except for the obliquity. Simulated LPs are shown on the left panel of Figure 10.

Next, we simulate NIRSPAO observations as follows. We convolve a template spectrum (see Section 4.3) with the mocked LP and multiply the convolution with telluric spectrum. The telluric spectrum is a convolution of a telluric template and a telluric LP that is measured simultaneously as the object LP (Wang et al. 2017). Finally, noise, which is the residual of modeling real data, is added to the mocked data. Using the residual as noise accounts for both photon noise and systematic noise such as detector noise and modeling error.

We then infer the obliquity by analyzing the mocked data with the package as described in Section 4. Posterior distributions of model parameters are shown on the right panel of Figure 10. With an input obliquity of −90°, the Bayesian inference returns an obliquity of $-94.1^{-14.0}_{+14.3}$ degree. Therefore, our inferred obliquity is consistent with the input value.

The uncertainty of obliquity for the mocked data is a factor of ∼2–3 smaller than the reported value from the real data. We attribute the difference to a few steps in our analysis. First, the template spectrum we use does not perfectly agree with the real spectrum for a low-mass star, but it is assumed that they match in simulation. Second, our analytic model to describe an LP is imperfect as it parameterizes the Doppler shadow as the maximum and minimum velocities of the occulted area (see Section 4.3), but in reality may be more complicated. The mismatch is not accounted for in our simulation. Lastly, we fix the y-axis scaling factor in the analysis for the mocked data. This is because LP normalization for mocked data has less uncertainty, which mainly comes from ripples outside the rotational broadening velocities. The real data show more ripples (Figure 9) than the mocked data (Figure 10), and therefore require an additional scaling factor to account for the normalization uncertainty.

Appendix B
Comparing the Analytic Model with the Finite-element Model

We compare our analytic model to a finite-element model that pixelates the stellar surface and numerically integrates it to calculate LPs (Albrecht et al. 2014, and references therein). Two cases are considered, one is a prograde orbit with $\lambda = 0°$ and the other case is a polar orbit $\lambda = -90°$. All model parameters, except for obliquity, are the same as what are assumed or inferred from EPIC 203868608 Bab. Both models assume no macro-turbulence, but the finite-element model assumes a micro-turbulence of 2 km s^{-1}. Micro-turbulence and macro-turbulence do not play a significant role in the EPIC 203868608 Bab case because the LP is mainly dominated by rotational broadening.

Figure 11 shows the comparison between the two models. In both the prograde and the polar orbits cases, the two models agree with each other within 7% of their maximum values. The disagreement between models is at most 38% of the LP measurement errors (light gray bars in Figure 11). This suggests that LP measurement uncertainties dominate the uncertainty in our obliquity inference. However, the disagreement between models will be a source of systematic error for future observations with higher S/N and lower LP measurement uncertainty. The

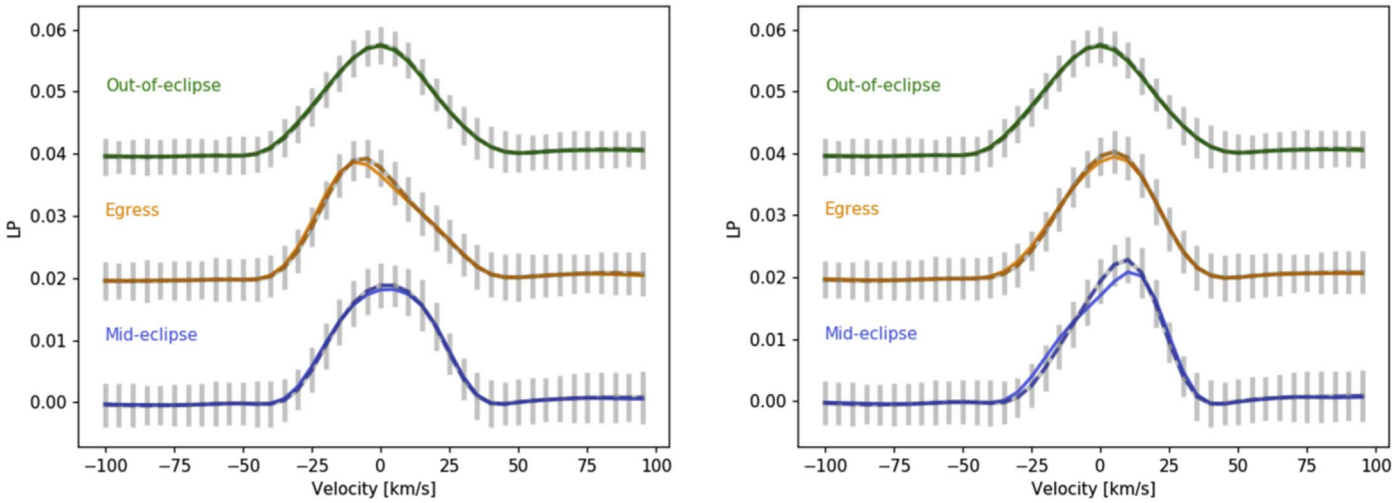

Figure 11. Left: comparison between our analytic model (dashed lines) and a finite-element model (solid lines, Albrecht et al. 2014, and references therein) for $\lambda = 0°$. The LP measurement errorbars are shown in light gray. Right: the same as the left except for $\lambda = -90°$.

comparison between models shows that the analytic model used here needs to be improved. This issue will be addressed in a future paper (J. M. Pezzato et al. 2018, in preparation).

ORCID iDs

Ji Wang https://orcid.org/0000-0002-4361-8885
Trevor J. David https://orcid.org/0000-0001-6534-6246
Dimitri Mawet https://orcid.org/0000-0002-8895-4735

References

Albrecht, S., Reffert, S., Snellen, I., Quirrenbach, A., & Mitchell, D. S. 2007, A&A, 474, 565
Albrecht, S., Winn, J. N., Torres, G., et al. 2014, ApJ, 785, 83
Allard, F., Hauschildt, P. H., Alexander, D. R., Tamanai, A., & Schweitzer, A. 2001, ApJ, 556, 357
Alonso, R., Deeg, H. J., Hoyer, S., et al. 2015, A&A, 584, L8
Asensio Ramos, A., & Petit, P. 2015, A&A, 583, A51
Baraffe, I., Homeier, D., Allard, F., & Chabrier, G. 2015, A&A, 577, A42
Batygin, K., & Adams, F. C. 2013, ApJ, 778, 169
Bishop, C. M. 1995, Neural Networks for Pattern Recognition (New York: Oxford Univ. Press)
Boden, A. F., Torres, G., Sargent, A. I., et al. 2007, ApJ, 670, 1214
Bodenheimer, P. 1978, ApJ, 224, 488
Boogert, A. C. A., Blake, G. A., & Tielens, A. G. G. M. 2002, ApJ, 577, 271
Borkovits, T., Hajdu, T., Sztakovics, J., et al. 2016, MNRAS, 455, 4136
Borucki, W. J., Koch, D., Basri, G., et al. 2010, Sci, 327, 977
Bowler, B. P., & Hillenbrand, L. A. 2015, ApJL, 811, L30
Carter, J. A., Fabrycky, D. C., Ragozzine, D., et al. 2011, Sci, 331, 562
Claret, A., Hauschildt, P. H., & Witte, S. 2012, A&A, 546, A14
Conroy, K. E., Prša, A., Stassun, K. G., et al. 2014, AJ, 147, 45
Cutri, R. M., Skrutskie, M. F., van Dyk, S., et al. 2003, yCat, 2246
David, T. J., Hillenbrand, L. A., Cody, A. M., Carpenter, J. M., & Howard, A. W. 2016, ApJ, 816, 21
Delgado-Donate, E. J., Clarke, C. J., Bate, M. R., & Hodgkin, S. T. 2004, MNRAS, 351, 617
Derekas, A., Kiss, L. L., Borkovits, T., et al. 2011, Sci, 332, 216
Duchêne, G., & Kraus, A. 2013, ARA&A, 51, 269
Fabrycky, D., & Tremaine, S. 2007, ApJ, 669, 1298
Follert, R., Dorn, R. J., Oliva, E., et al. 2014, Proc. SPIE, 9147, 914719
Foreman-Mackey, D., Hogg, D. W., Lang, D., & Goodman, J. 2013, PASP, 125, 306
Gaia Collaboration, , Brown, A. G. A., Vallenari, A., et al. 2018, A&A, 616, A1
Ghez, A. M., Neugebauer, G., & Matthews, K. 1993, AJ, 106, 2005
Goodman, J., & Weare, J. 2010, Communications in Applied Mathematics and Computational Science, 5, 65
Hillenbrand, L. A., & White, R. J. 2004, ApJ, 604, 741
Hirano, T., Suto, Y., Winn, J. N., et al. 2011, ApJ, 742, 69
Horch, E. P., Howell, S. B., Everett, M. E., & Ciardi, D. R. 2014, ApJ, 795, 60
Howell, S. B., Sobeck, C., Haas, M., et al. 2014, PASP, 126, 398
Hut, P. 1981, A&A, 99, 126
Johnson, M. C., Cochran, W. D., Albrecht, S., et al. 2014, ApJ, 790, 30
Kirk, B., Conroy, K., Prša, A., et al. 2016, AJ, 151, 68
Kotani, T., Tamura, M., Suto, H., et al. 2014, Proc. SPIE, 9147, 914714
Kozai, Y. 1962, AJ, 67, 591
Kraus, A. L., Cody, A. M., Covey, K. R., et al. 2015, ApJ, 807, 3
Lehmann, H., Borkovits, T., Rappaport, S. A., et al. 2016, ApJ, 819, 33
Lehmann, H., Zechmeister, M., Dreizler, S., Schuh, S., & Kanzler, R. 2012, A&A, 541, A105
Lidov, M. L. 1962, P&SS, 9, 719
Lodieu, N., Alonso, R., González Hernández, J. I., et al. 2015, A&A, 584, A128
Martin, E. C., Fitzgerald, M. P., McLean, I. S., et al. 2014, Proc. SPIE, 9147, 914781
Mathieu, R. D. 1994, ARA&A, 32, 465
Mathieu, R. D., Baraffe, I., Simon, M., Stassun, K. G., & White, R. 2007, in Protostars and Planets V, ed. B. Reipurth, D. Jewitt, & K. Keil (Tucson, AZ: Univ. Arizona Press), 411
Matsumura, S., Takeda, G., & Rasio, F. A. 2008, ApJL, 686, L29
Mawet, D., Wizinowich, P., Dekany, R., et al. 2016, Proc. SPIE, 9909, 99090D
McLaughlin, D. B. 1924, ApJ, 60, 22
Peale, S. J. 1999, ARA&A, 37, 533
Pineda, J. E., Offner, S. S. R., Parker, R. J., et al. 2015, Natur, 518, 213
Piskorz, D., et al. 2016, ApJ, 832, 131
Pont, F., Hébrard, G., Irwin, J. M., et al. 2009, A&A, 502, 695
Raghavan, D., McAlister, H. A., Henry, T. J., et al. 2010, ApJS, 190, 1
Rappaport, S., Lehmann, H., Kalomeni, B., et al. 2016, MNRAS, 462, 1812
Rappaport, S., Vanderburg, A., Borkovits, T., et al. 2017, MNRAS, 467, 2160
Rasio, F. A., Tout, C. A., Lubow, S. H., & Livio, M. 1996, ApJ, 470, 1187
Rauer, H., Catala, C., Aerts, C., et al. 2014, ExA, 38, 249
Reipurth, B., & Mikkola, S. 2012, Natur, 492, 221
Ricker, G. R., Winn, J. N., Vanderspek, R., et al. 2014, Proc. SPIE, 9143, 20
Rossiter, R. A. 1924, ApJ, 60, 15
Shkolnik, E., Liu, M. C., Reid, I. N., et al. 2008, ApJ, 682, 1248
Spalding, C., & Batygin, K. 2014, ApJ, 790, 42
Stassun, K. G., Feiden, G. A., & Torres, G. 2014, NewAR, 60, 1
Sterzik, M. F., & Durisen, R. H. 1998, A&A, 339, 95
Tobin, J. J., Kratter, K. M., Persson, M. V., et al. 2016, Natur, 538, 483
Tohline, J. E. 2002, ARA&A, 40, 349
Tokovinin, A. 2008, MNRAS, 389, 925
Tonry, J., & Davis, M. 1979, AJ, 84, 1511
Torres, G., Ruíz-Rodríguez, D., Badenas, M., et al. 2013, ApJ, 773, 40
Vogt, S. S., Allen, S. L., Bigelow, B. C., et al. 1994, Proc. SPIE, 2198, 362
Wang, J., Prato, L., & Mawet, D. 2017, ApJ, 838, 35
White, R. J., Ghez, A. M., Reid, I. N., & Schultz, G. 1999, ApJ, 520, 811
Wizinowich, P. L., Acton, D. S., Lai, O., et al. 2000, Proc. SPIE, 4007, 2
Wright, J. T., & Eastman, J. D. 2014, PASP, 126, 838
Yelda, S., Lu, J. R., Ghez, A. M., et al. 2010, ApJ, 725, 331